FAR ULTRAVIOLET IMAGING FROM THE IMAGE SPACECRAFT: 1. SYSTEM DESIGN

S. B. MENDE, H. HEETDERKS, H. U. FREY, M. LAMPTON, S. P. GELLER
Space Sciences Laboratory, University of California Berkeley, Berkeley, CA 94720
S. HABRAKEN, E. RENOTTE, C. JAMAR, P. ROCHUS
Centre Spatiale de Liege, Liege, Belgium B-4031
J. SPANN
George C. Marshall Spaceflight Center, Huntsville, AL 35812
S. A. FUSELIER
Lockheed Martin Advanced Technology Center, Palo Alto, CA, 94304
J.-C. GERARD
University of Liege, Liege, Belgium B-4000
R. GLADSTONE
Southwest Research Institute, San Antonio, Texas 78228
S. MURPHREE, L. COGGER
University of Calgary, Calgary, Canada AB T2N 1N4

Abstract. Direct imaging of the magnetosphere by the IMAGE spacecraft will be supplemented by observation of the global aurora, the footprint of magnetospheric regions. To assure the simultaneity of these observations and the measurement of the magnetospheric background neutral gas density, the IMAGE satellite instrument complement includes three Far Ultraviolet (FUV) instruments. In the wavelength region 120-190 nm, a downward-viewing auroral imager is only minimally contaminated by sun light, scattered from clouds and ground, and radiance of the aurora observed in a nadir viewing geometry can be observed in the presence of the high-latitude dayglow. The Wideband Imaging Camera (WIC) will provide broad band ultraviolet images of the aurora for maximum spatial and temporal resolution by imaging the LBH N_2 bands of the aurora. The Spectrographic Imager (SI), a monochromatic imager, will image different types of aurora, filtered by wavelength. By measuring the Doppler-shifted Lyman-α, the proton-induced component of the aurora will be imaged separately. Finally, the GEO instrument will observe the distribution of the geocoronal emission, which is a measure of the neutral background density source for charge exchange in the magnetosphere. The FUV instrument complement looks radially outward from the rotating IMAGE satellite and, therefore, it spends only a short time observing the aurora and the Earth during each spin. Detailed descriptions of the WIC, SI, GEO, and their individual performance validations are discussed in companion papers. This paper summarizes the system requirements and system design approach taken to satisfy the science requirements. One primary requirement is to maximize photon collection efficiency and use efficiently the short time available for exposures. The FUV auroral imagers WIC and SI both have wide fields of view and take data continuously as the auroral region proceeds through the field of view. To minimize data volume, multiple images are taken and electronically co-added by suitably shifting each image to compensate for the spacecraft rotation. In order to minimize resolution loss, the images have to be distortion-corrected in real time for both WIC and SI prior to co-adding. The distortion correction is accomplished using high speed look up tables that are pre-generated by least square fitting to polynomial functions by the on-orbit processor. The instruments were calibrated individually while on stationery platforms, mostly in vacuum chambers as described in the companion papers. Extensive ground-based testing was performed with visible and near UV simulators mounted on a rotating platform to estimate their on-orbit performance. The predicted instrument system performance is summarized and some of the preliminary data formats are shown.

1. Introduction

Magnetospheric science aims to understand how charged particles, magnetic fields, and electric fields interact with each other and how these interactions are modulated by external influences, such as the solar wind and its magnetic field. During the past 40 years, spacecraft-borne monitoring instruments, which made localized (in situ) measurements of magnetospheric particles and fields, have studied the magnetosphere. The IMAGE spacecraft investigation will be the first space borne program to observe the magnetosphere by remote sensing techniques only. The IMAGE spacecraft carries several imagers that use novel techniques to see the plasma in the magnetosphere from a remote location. By imaging the He II ultraviolet line in the magnetosphere at 30.4 nm, IMAGE will directly image the ionized Helium content of cold plasma surrounding the Earth and monitor how the cold plasma responds

to changes in the interplanetary fields or substorm effects. By measuring neutral particle fluxes in various energy ranges, the IMAGE spacecraft will be able to study the plasma content of various regions (Roelof *et al.*, 1985; Roelof 1987; Williams *et al.*, 1992; Lui *et al.*, 1996; Jorgensen *et al.*, 1997). The observed neutral fluxes are produced by magnetospheric ions charge exchanging with the background neutral gas, and in the process the resultant fast neutrals carry the kinetic properties of the parent ion. Three types of neutral imagers will be flown on IMAGE to cover the different energy ranges of greatest interest in magnetospheric physics. The spacecraft will carry a magnetospheric radio sounder that will probe the magnetospheric plasma by radio sounding techniques. It is widely held that features of the polar aurora represent foot prints of magnetospheric boundaries and simultaneous observation of the global aurora will provide important context information to supplement direct imaging of the magnetosphere. To assure that simultaneous auroral observations are made and that the background neutral gas density is measured, several far ultraviolet imagers will also operate on the IMAGE spacecraft.

Previously flown satellite imaging experiments have demonstrated the suitability of the vacuum ultraviolet spectral region for remote sensing observation of auroral precipitation (Anger *et al.*, 1987; Frank *et al.*, 1981; Frank and Craven; 1988, Murphree *et al.*, 1994; Torr *et al.*, 1995). In the wavelength region 120-190 nm, a downward-viewing imager is minimally contaminated by scattered sun light from clouds and the ground. The radiance of the aurora observed in a nadir viewing geometry can be distinguished from the high-latitude dayglow. The UV emissions permit quantitative imaging of the auroral region. An instrument for such observation should also have adequate wavelength resolution to separate key spectral features and, preferably, high enough spectral resolution to be sensitive to the Doppler profile and distinguish the auroral Lyman-α line. The auroral Lyman-α line provides a measure of the auroral ion precipitation, which is proportional to the flux of protons precipitating into the atmosphere.

In general, an imager is a remote sensing instrument that makes multiplexed measurements of photon (particle) fluxes simultaneously from several distinct directions. This is usually done by having a single aperture collecting the light from several directions and an optical system that sorts the photons into appropriate buckets, or pixels, according to the direction of arrival. To a first order, imagers can be characterized primarily by the following general considerations: (1) the ability to define the mean direction of the light entering a pixel bucket, (2) the spatial size of the region associated with a pixel, (3) the efficiency of counting the photons within the pixel, and (4) the acceptance or rejection of photons based on their wavelength properties.

(1) Positions are usually defined by characterizing the mean direction of the arriving beam of photons collected into a pixel. This is usually handled by defining a reference or optic axis of the imager in inertial space on the satellite and characterizing the image distortion by making relative angular measurements of the incident beam from this axis.

(2) Resolution or size of the pixels is determined by the measurement of the relative response of one pixel to photons arriving from various directions.

(3) The efficiency of an imager is characterized by measuring the number of counts, which contribute to the signal associated with a pixel. When a known number of photons, P per square cm arrive at the input aperture during the exposure time the output signal to noise ratio (SNR) is measured. From the output signal to noise ratio it is possible to calculate the number of equivalent output quanta (Q), which would produce the same output signal to noise ratio through Poisson statistics i.e. $(SNR)^2 = Q$. The ratio of the output quanta to the input photons, Q/P is the efficiency of the imager. The product of the efficiency of the detector and the area of the collecting aperture is the equivalent collecting area, A_e of an imager.

(4) The spectral response of the instrument is the dependence of its efficiency on photon wavelength. In most FUV instruments, the spectral band is limited by the optical properties and materials, but additional filters and spectral gratings can be used to limit the wavelength band of transmission. Since most FUV imaging will be done in the presence of some solar illumination, it is of utmost importance to minimize out of band contributions.

The intensity unit, Rayleigh, is used most often in the measurement of terrestrial aurora. A Rayleigh is equivalent to a source strength in which a 1 cm^2 area integrated line of sight column of aurora emits 10^6 photons s^{-1} in 4π strd (Hunten *et al.*, 1956). Thus, a Rayleigh is $10^6/4 \pi \sim 80,000$ photons s^{-1} cm^{-1} $strd^{-1}$. To express the intensity response of an imager in terms of equivalent output count Q per Rayleigh, one needs to multiply the field of view in steradian, the exposure duration in seconds and the equivalent collecting area, A_e by 80,000. Note that the field of view and the exposure time are generally defined by factors outside of the instrument, such as the spatial and temporal scale of the phenomena and the properties of the platform from which the observation is performed. In determining the efficiency, the instrument can be characterized solely by the equivalent collecting area A_e.

2

In this paper we shall identify the requirements as derived from the mission science goals and the constraints associated with the IMAGE observing platform. We shall describe the design approach taken for the overall FUV system. We will provide a detailed description of the individual instruments and their calibration in two companion papers. In the first of the companion papers (paper #2) we describe the Wideband Imaging Camera (WIC), and in the other (paper#3) the Spectrographic Imager (SI) and the Geocorona Photometers (GEOs). Although the detailed calibration will be discussed in the companion papers, we will summarize the calibration results and the initial data formats planned for the IMAGE FUV system.

2. IMAGE FUV Requirements

The IMAGE program scientific goals can be summarized in three questions; (1) What are the dominant mechanisms for injecting plasma into the magnetosphere on substorm and magnetic storm time scales? (2) What is the directly driven response of the magnetosphere to solar wind changes? and (3) How and where are magnetospheric plasmas energized, transported, and subsequently lost during storms and substorms? For several decades, the search for answers to these questions were conducted using spacecraft-born, single point in situ measurements. Simultaneous multi-point measurements are needed to make substantial progress (Williams, 1990). The IMAGE spacecraft will make remote sensing (imaging) observations of all regions of the magnetosphere simultaneously.

The FUV auroral instrument complement will provide global images of the auroral oval to allow comparisons of the auroral data to the magnetospheric IMAGE data. The location and shape of the auroral regions are important indicators of magnetospheric conditions providing important context information for all the IMAGE measurements. It is, therefore, a primary requirement of IMAGE FUV to cover the entire auroral oval from apogee. In fact, the Earth subtends a total of about 16° from IMAGE apogee and the auroral oval is about 8°.

The aurora is a product of magnetospheric particle and energy loss mechanisms. Therefore, FUV contributes more directly to question number 3. However, the following issues will be addressed using the IMAGE FUV instruments:

(1) Mechanism for injecting plasma into the magnetosphere.

During conditions of IMF Bz southward, magnetosheath particles can enter the magnetosphere through the dayside boundary layer (Fuselier *et al.*, 1991). During positive Bz, the situation is more complex because the reconnection process occurs in regions other than the dayside near the sub-solar point and the convection driving the plasma is much less understood. IMAGE will provide an opportunity to observe the dayside entry region with MENA and RPI, while FUV will monitor the size, intensity and location of the dayside electron and proton precipitation, and we will be able to map the foot print of the dayside entry region. The location and intensity of the ion outflow (Lockwood *et al.*, 1985; Pollock *et al.*, 1990) will be observed by LENA, while the FUV package will determine the related auroral activity in the dayside region. To locate the position of the aurora to an accuracy of about 1° (of latitude) resolution consistent with 100 km pixels is desirable.

(2) Directly driven response of the magnetosphere to solar wind and IMF field.

Magnetopause erosion. The inward displacement, or erosion, of the dayside magnetopause and the predicted flaring of the tail magnetopause during the substorm growth phase (Coroniti and Kennel, 1972) will be observed by the RPI while FUV will monitor the substorm development on the nightside. FUV will observe the simultaneous position, extent, and form of the auroral foot print, while MENA and RPI will determine the position of the magnetosheath plasma on the dayside. We should be able to track directly the motions of the aurora and the magnetosheath plasma as the magnetosphere changes shape through magnetic erosion, responds to solar wind pressure, and reacts to the substorm phases. Auroral bright spots of a few hundred km in size seen on the dayside have been associated with Kelvin-Helmholtz instabilities on the low latitude boundary layer (LLBL) (Lui *et al.*, 1989). The plasma will be observed by the neutral atom imagers and by RPI, while FUV will record the corresponding periodic structures seen in the aurora. To see the auroral bright spots of the size and intensity seen by the VIKING camera (Lui *et al.*, 1989), a resolution consistent with 100 km pixel size is adequate and an intensity equivalent to about 2 kR of 427.8 nm is needed (~ 10 erg). This is equivalent to several kR of 135.6 nm (Strickland *et al.*, 1983).

Plasmaspheric Processes. IMAGE will observe the plasmaspheric ions by making images of the EUV resonance scattering and RPI soundings of the magnetospheric plasma inside the orbit. FUV will monitor the location and extent of the precipitation. Comparing these data sets, it will be possible to determine what effect the presence of cold plasmaspheric ions has on the precipitation of particles from the magnetosphere.

(3) Energization and loss of magnetospheric plasmas.

Substorm Plasma Injection. The neutral imagers will be able to observe inward motion of substorm injection fronts and FUV will report on the simultaneous auroral substorm phenomena such as arc formation, substorm poleward expansions and recovery. The neutral imagers will show how the injected plasma is accelerated and how it redistributes in the magnetosphere. Once again, FUV will provide the global distribution of the simultaneous precipitation, providing a measure of the fraction of particles that have acquired pitch angles that fall inside the loss cones. The precipitation of particles due to wave scattering by pitch angle diffusion represents one of the most significant loss mechanisms of the ring current.

Thus, a primary requirement of IMAGE FUV is global coverage of the auroral oval from geocentric distances of near orbit apogee of 44, 000 km. From the IMAGE orbit apogee the solid Earth subtends about 16°. In the IMAGE FUV design, the WIC camera and the SI have 17° x 17° and 15° x 15° field of views. These instruments will cover an area of 13,300 x 13,300 and 11,700 x 11,700 km respectively at 7 R_E distance. This way the entire auroral oval will be covered when the satellite altitude is greater than 4 to 5 R_E.

The required resolution can be obtained by considering that it is desirable to see features that are on the order of 100 km in size. It was necessary to have at least a 128 x 128 pixel raster to cover the entire field. To satisfy this requirement, the WIC design had a 256 x 256 nominal pixel field and SI had 128 x 128 pixel detectors. The projection or "foot print" of such a nominal pixel at 7 R_E distance is 92 x the SI and 52 x 52 for the WIC. For 1000 km perigee observations from IMAGE orbit, the nominal pixel sizes are 1.2 and 2 km for the WIC and SI, respectively.

Once the pixel size is defined we can calculate the solid angle subtended by each pixel, which is about 1.3×10^{-6} and 4.2×10^{-6}, respectively for WIC and SI. As discussed previously, the photon collection efficiency per Rayleigh of any imager viewing pixels with a pixel solid angle of 1.3×10^{-6} is intrinsically limited to $80,000 \times 1.3 \times 10^{-6} = 0.1$ photons s^{-1} Rayleigh^{-1} for each square cm of input aperture. Similarly for an SI pixel, the photon collection efficiency is 0.33 photons s^{-1} Rayleigh^{-1} cm^{-2}. From the desired S/N and the available auroral intensity we can calculate the desired equivalent aperture for the instrument, A_e.

The FUV instruments must fulfill the following requirements: (a) Image the aurora in conditions of polar dayglow, (b) Observe the proton precipitation component of the aurora, and (c) Measure the geocoronal Lyman-α. The latter data will be needed to interpret the IMAGE neutral atom imaging measurements because they provide the magnetospheric geocoronal hydrogen density responsible for charge exchange. FUV needs several sensors to fulfill these requirements. On the IMAGE mission there are three.

The Wideband Imaging Camera (WIC) will provide broad band ultraviolet images of the aurora for maximum spatial and temporal resolution day and night. The Spectrographic Imager (SI) will make quantitative two-dimensional images of different types of aurora, filtering them by wavelength. By measuring the Doppler-shifted Lyman-α the proton-induced auroras will be imaged separately from electron precipitation aurora at other wavelengths. Finally, the GEO instrument will observe the distribution of the geocoronal emission. The hydrogen distribution around the Earth will be modeled (Hodges 1994; Bishop 1999), and the model parameters will be adjusted to agree with the GEO measurements.

A typical modeled auroral spectrum for average nightside aurora (10 kR of 1304) (courtesy of R. L. Gattinger) in the ultraviolet is shown in Figure 1. Progressing from left to right, Lyman-α at 121.6 nm has two components. The cold Lyman-α at 121.5667 nm is produced by the geocorona and the hot, Doppler-shifted auroral Hydrogen emission is produced by protons precipitating into the atmosphere. Because of the charge exchange process, protons pick up an electron and there is a high probability that they end up in the upper state of the Lyman-α transition. When they spontaneously decay, the resulting radiation will be Doppler-shifted (by several Angstroms) because they move primarily away from an observer located at the apogee of the IMAGE satellite. The IMAGE FUV spectrographic imager SI12 channel observes this emission.
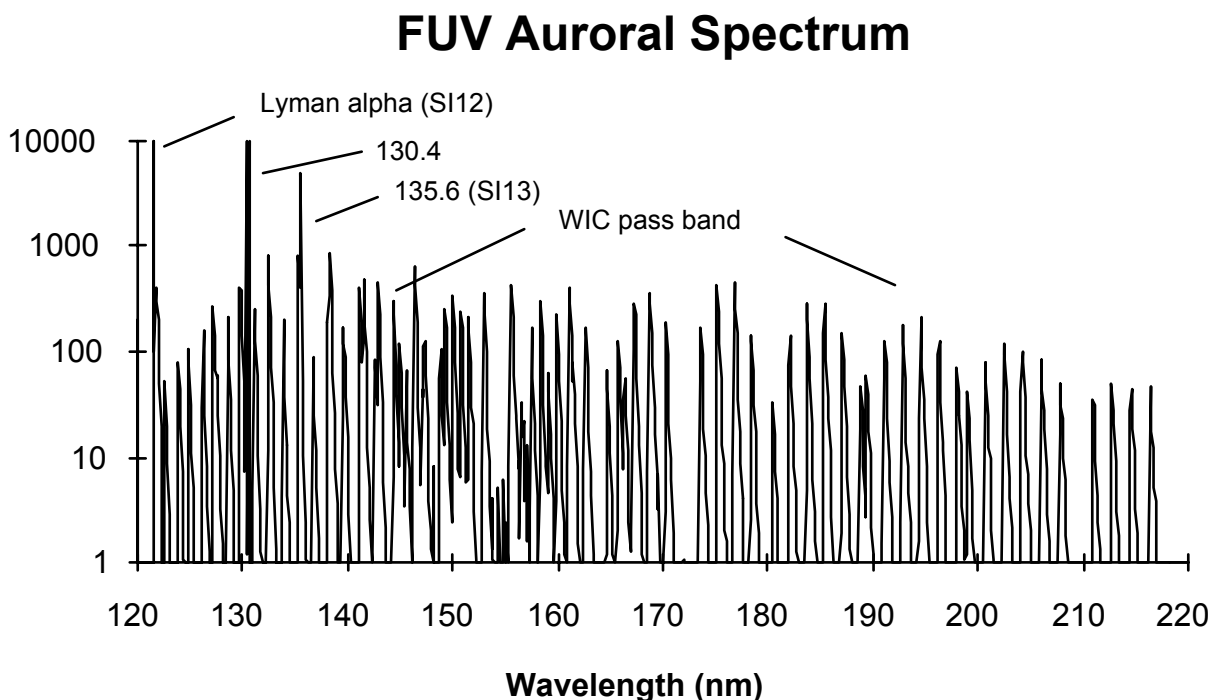
FUV Auroral Spectrum

Figure 1. The Spectral modeling of the ultraviolet auroral emissions and the geocorona. (Courtesy of R. L. Gattinger). The model is typical nightside aurora with 10 kR intensity of OI 130.4 nm.

There are several auroral emission features as or more intense than the dayglow in the FUV range. The spectrally diffuse dayglow in the FUV region (Meier, 1991) from 100 to about 170 nm is less than 100 Rayleighs per nm when viewed in the fully illuminated nadir. Intensity increases 2 orders of magnitude above the 170 nm dayglow, so it is particularly important to suppress emissions in the wavelength range 170 nm and higher. There are strong Lyman-α, 130.4 and 135.6 nm dayglow emissions. Most auroral imaging of the polar atmosphere will take place when the solar illumination is at a slant angle and the dayglow contribution is much reduced.

Although the brightest line in the aurora is the 130.4 OI emission, it is multiply scattered in the atmosphere and it is difficult to obtain a two-dimensional intensity distribution of the auroral source. The 135.6 nm line is scattered only to a limited degree (Strickland and Anderson, 1983b) and, therefore, provides an excellent emission feature for imaging the aurora and relating it to the total precipitation. Thus, an important measurement requirement is the detection and spectral separation of the 135.6 nm emission from the 130.4. For example, the transmission of the instrument at 130.4 nm should be less than 1% of its 135.6 nm transmission. This requirement necessitated the use of a spectrometer because today's FUV narrow band filter technology is not able to satisfy this requirement. A specific wavelength channel, the SI13 channel will image this emission feature.

Weak lines of the FUV Lyman-Birge-Hopfield (LBH) system populate the rest of the FUV region, which are excited primarily by electrons on N_2. A method for obtaining precipitating electron parameters from FUV observations is outlined by Strickland *et al.* (1983; 1993). Atmospheric O_2 is an absorbing agent residing in the lower part of the atmosphere, and emissions in the mid FUV wavelength region, coming from deeper in the atmosphere, tend to get absorbed by it. The O_2 absorption becomes less significant in the longer (>160 nm) wavelength range.

Thus, comparison of the emission intensities at lower and higher wavelengths within the FUV region yields a parameter that can be related to the altitude of emission, and taking it one step further, to the energetics of the

precipitating electrons. By inverting the relationship between the ratios of the emissions it is possible to obtain the electron flux and mean energy of the precipitating electrons.   The FUV emissions are most effective in discriminating particle energies in the region 1-5 keV. Electrons in the energy range below 1 keV create auroral processes that take place above the bulk of the O_2 layer and there is little sensitivity to energy. Above 5-10 keV the emissions are strongly absorbed once again, inhibiting the discrimination of the energies. It was decided early in the planning of the IMAGE mission that we would have only one broad band LBH imager to image the auroral LBH, and not use the energy determination technique of comparing high and low wavelength LBH.

In the absence of the two channel LBH measurements, it would be possible to compare the measured (line of sight integral) OI 135.6 nm and LBH system intensity and, in principle, estimate the O_2 absorption and infer the altitude of the precipitation, hence, the energy of the precipitating electrons. LBH and 135.6 OI are produced by electron impact on N_2 and O, respectively. Therefore, energy estimates of the precipitating electrons based on their auroral column emission ratios would have to rely on the assumption that the N_2/O ratio of the atmosphere is constant. This ratio, however, is a variable and strongly dependent on magnetospheric activity (e.g. Strickland *et al.*, 1999). In the absence of the energy measurements it will be necessary to make an assumption regarding the mean energy of each auroral feature and infer the auroral energy flux from the emission intensities (e.g. Strickland *et al.*, 1983).

The hydrogen atom geocorona is an important region for several of the instruments on IMAGE. Charge exchange between hot magnetospheric plasma and ambient H atoms in outer parts of the geocorona provide most of the energetic neutral atoms observed by the neutral atom imagers. The solar Lyman-α radiation scattered by the geocorona is also a source of undesirable background for the FUV/SI-1216 instrument, which is designed to image proton auroras. The FUV/GEO instrument will be used to characterize the geocorona so that charge-exchanging ion fluxes can be determined from the neutral atom signals.

As with the DE-1 studies of the geocorona (e.g., Rairden *et al.*, 1986), IMAGE will observe the scattered solar Lyman-α radiation to determine the distribution and dynamics of H atoms from the upper thermosphere out to several Earth radii, where the signal becomes lost in the interplanetary background (e.g., Ajello *et al.*, 1990). Recent improvements in modeling of the Lyman-α geocorona (e.g., Hodges 1994; Bishop 1999) will allow simulations, which can be compared to the data allowing the study of, e.g., seasonal and tidal asymmetries, or "comet-like" tail structures, as they are detected.

Since the orbital plane of IMAGE will not precess during the mission, the FUV/GEO instrument will always have the same view of the interplanetary medium (IPM) background Lyman-α emission. However, the IPM signal will vary during the year as the Earth moves from upstream to downstream and back with respect to the interstellar wind.

Earth's FUV dayglow emissions comprise all of the same spectral features seen in the FUV emissions, only excited by photoelectrons rather than the typically much higher energy precipitating auroral particles and secondary electrons. Resonant scattering of sunlight can also be important, as in the case of the OI 130.4 nm triplet (Meier, 1991). The OI 135.6 nm and N_2 LBH emissions that FUV will monitor in the auroral regions also have large, photoelectron-generated dayglow components. Since the solar EUV radiation source responsible for photoelectron production varies relatively slowly over the dayside hemisphere, any small to medium scale structure observed in images of the FUV dayglow can be related to local compositional variations (Immel *et al.*, 1997). For example, by ratioing images of OI 135.6 nm emission to images of N_2 LBH emission, we can effectively provide maps of the N_2/O ratio in the lower thermosphere (Gladstone, 1994, Strickland et al., 1995). These types of ratio images can be used to study the effect of auroral activity on the composition and dynamics of the thermosphere at non-auroral latitudes (e.g., Strickland *et al.*, 1999; Drob *et al.*, 1999). Thus, the FUV observations of the dayglow may be used to infer the impact of auroral events on a more global scale.

Non-auroral aspects of the FUV airglow may also be investigated, of course. For instance, 1) the response to solar flares or other sudden changes in the EUV output of the sun, 2) the effect of conjugate region precipitation of photoelectrons, 3) recombination of O^+ ions in the tropical nightglow, and even 4) searches for the signatures of small comet impacts (cf. Frank and Sigwarth, 1999). Many of these phenomena can be well studied by IMAGE, either with nadir viewing at apogee or by limb viewing at perigee.

Imaging the magnetosphere in neutral atoms requires very wide fields of view. This is accomplished by wide field of view imaging in one dimension, in the direction parallel to the satellite spin axis, and complete coverage in the other dimension is accomplished by rotating the satellite around its axis.   On IMAGE, all the instruments view radially outward away from the spin axis. The spin axis was chosen to be perpendicular to the orbit plane. The orbit is truly polar (90° orbital inclination) with apogee at 44,000 km and perigee at 1000 km. For the first two years of

the mission, apogee is over the Northern Hemisphere and directly above the pole after one year. The satellite will spend most of its time far away from the Earth observing at and near apogee. The FUV auroral instruments view the Earth for a brief time– once per satellite revolution (period of revolution = 2 min.).

Table 1
IMAGE FUV Requirement Summary

	Wave-length (nm)	FOV (°)	Pixel size apogee (km)	Angular resolution (°)	Photon collection efficiency times (exposure time) (Rayleigh^{-1} pix^{-1} cm^{-2})	Minimum Aperture for 1 count pix^{-1} for 100 R source strength (cm^2)
LBH Auroral morphology	140-90	>10	100	0.13	4.1 (10 s)	0.0024
OI auroral morphology	135.6 with <1% 130.4 rejection	>10	100	0.13	1.65 (5 s)	0.006
Hydrogen aurora	121.8+-0.1 with 1215.667 rejection	>10	200	0.26	6.6 (5 s)	0.0015
Geocorona	121.6	360	N/A	1.0	5 (0.33 s)	0.002
Dayglow	LBH and 135.6	>10	200	0.26	6.6 (5 s)	0.0015

The FUV requirements are summarized in Table 1. The first column presents the broad science object, the second column shows the relevant wavelength region. The field of view (FOV) is derived from the global coverage requirement of the aurora near perigee. In the case of the geocorona it is a 360° coverage. The science objective defines the ground resolution, which translates into an angular resolution listed in column five. As was discussed earlier, the angular resolution defines the photon collection efficiency of the imager in photons Rayleigh^{-1} pix^{-1} cm^{-2} s^{-1}. The FUV images are taken on a rotating spacecraft and the rotation rate is 3° per second (one revolution in every two minutes). The field of view was chosen to be 15° for the SI instrument and 30° for the WIC in the direction of rotation. Each auroral feature, therefore, spends 5 seconds in the SI FOV and 10 seconds in the WIC FOV. This consideration defines the exposure time. We have included the exposure time and provide the data for the photon collection efficiency for one exposure, or one rotation of the spacecraft, in the column representing photon collection efficiency. The last column is the required equivalent aperture for the instrument to provide one count per pixel for a 100 Rayleigh auroral source. These apertures look rather small but we have to realize that they include the actual collecting aperture of the instrument multiplied by the combination of optical transmissions and the applicable efficiencies of conversion of photons into measurable electric charge units. The combined efficiencies for ultraviolet instruments is usually no more than 1 to 2%.

In addition, the various contaminant emissions contribute significantly to the minimum detectable signal. Thus, one count per pixel may be sufficient to produce an acceptable image in the absence of any background. In the presence of a background, larger signal to noise is required. In summary, we have demonstrated the need for instruments with large apertures and high efficiency for IMAGE FUV.

The IMAGE spacecraft orbit is highly eccentric, apogee distance being at 7 Re while the perigee altitude is 1000 km. The satellite crosses the radiation belts on each orbit and relatively high radiation environment is experienced by the satellite. Modeling of the radiation environment showed that inside the electronics enclosures which had 0.2 inch thick aluminum walls the electronics would experience a dose of 50 kRad in 2 years. CCD-s are significantly affected by energetic protons flux because their charge transfer efficiency is impaired due to proton induced charge trap generation. The WIC design called for the use of a CCD. Modeling of the proton fluence resulted in a

requirement to specially shield the CCD and eliminate protons which have less than 50 MeV energy. The CCD shielding design required a small Tantalum cup weighing about 500 gm.

3. The IMAGE FUV System

The greatest challenge the IMAGE FUV instrument faces is the difficulty of taking high resolution and high sensitivity images during the short period when the FUV imagers sweep by the Earth. The two SI detectors and the WIC are capable of producing full two-dimensional images in a staring mode. However, they will be operating on a rotating platform in flight in a manner analogous to taking pictures of a stationary object in quick succession while on a rotating carousel with a mounted camera pointing radially outwards. To take advantage of the entire period that FUV is looking at the aurora, the FUV images are processed by superimposing all the images, suitably offsetting from one to the next to compensate for spacecraft rotation. This method of processing is called Time Delay Integration (TDI).

The observing scheme is illustrated in Figure 2. The Earth subtends about 16° at apogee and the field of view swings through the Earth direction once per spacecraft rotation. The middle diagram illustrates the principle of TDI. The technique satisfies two requirements: 1) It maximizes the signal to noise ratio, 2) it minimizes the spacecraft telemetry by storing and transmitting only one single image per rotation. The illustration shows the rotating satellite and the instrument memory, which is used to store the information. The memory is an array of cells with each cell assigned a certain look angle fixed in space. The total angular field is assigned to the complete memory matrix, and is shown as the "memory FOV". As the spacecraft rotates, the instantaneous field of view of the imager will be sampling a portion of the memory FOV and the output image is taken by scanning the imager instantaneous FOV across the memory FOV.

Imager instantenous FOV

Memory FOV

Direction of rotation

Imager FOV (distorted)

x_1

x_0

ωt

Imager FOV (undistorted)

x_2

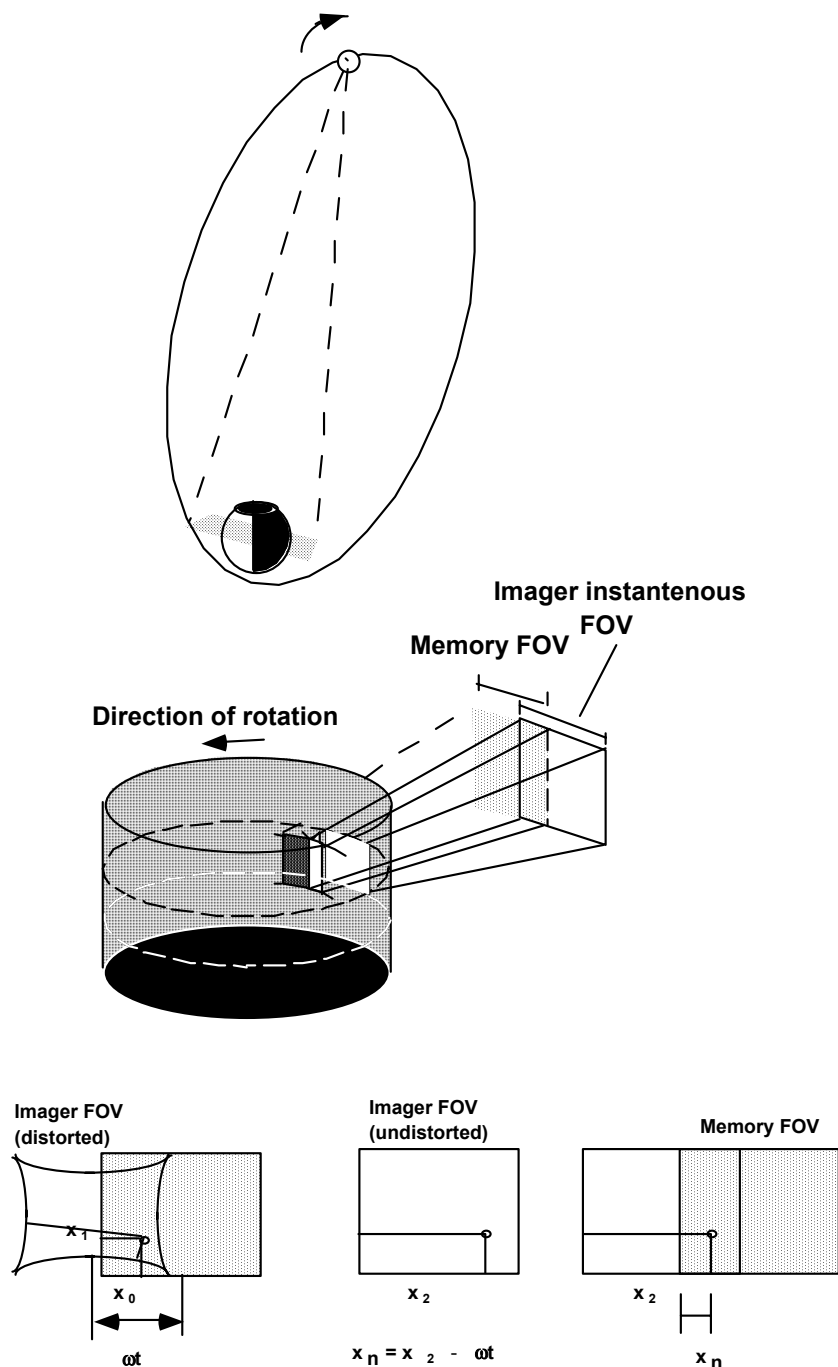$x_n = x_2 - \omega t$

Memory FOV

x_2

x_n

Figure 2. Sketch of IMAGE eccentric polar orbit showing how the FUV imagers see the earth once per satellite spin period (top), the concept of TDI imaging on a rotating platform and the necessity of co-adding the information from the same region of space in memory (middle) and the distortion correction requirement (bottom).

The bottom illustration also shows the same process but in a plane view. At a time t, the imager field of view will be offset from the memory field of view by an angle Kt, where K is the angular rotation rate. A pixel described by angular coordinates x_0, y_0 (only x_0 is shown in the figure) in inertial space will produce photons in the imager at pixel location x_1, y_1. Note that the imager usually distorts the image to some degree, illustrated here with some exaggeration. Since the images are co-added and the shift between instantaneous images is constant, all distortions and non-linearities must be removed. The output memories attached to the SI and WIC detectors are 128 x 128 and

256 x 256 pixels, respectively. From the above discussion it is evident that the TDI process including the distortion correction and rotation compensation requires a sophisticated real time, on-board image processing system.

As discussed earlier, both the SI and the WIC operate in the TDI mode. The WIC has a 30° field of view in the direction parallel to the plane of rotation. Therefore, a point on Earth spends approximately 30 x 120 /360 s = 10 s in the WIC field of view during each spin (2 minute spin period) defining the exposure. Each individual video field is about 1/30 s and a complete WIC exposure is a collage of approximately 300 video frames. Unfortunately, the rest of the time, 110 out of 120 s, the WIC imager is idly looking away from the Earth.

The field of view of both SI detectors is 15° x 15°. Each point on the Earth spends only 5 seconds in the SI field of view. Since the SI detectors are crossed delay line, single photon counting detectors the TDI scanning is done by modifying the address of each recorded photo electron. Although the two systems operate differently– the WIC processes whole frames and the SI processes individual photons– they are both subject to the basic considerations of the TDI process including distortion correction.

The FUV instrument block diagram is shown in Figure 3. The four packages in order of size are the Spectrographic Imager (SI) the Wideband Imaging Camera (WIC), the Main Electronic Package (MEP) and the Geocoronal Detector (GEO). The Wideband Imaging Camera consists of an ultraviolet wide-field optical system, followed by a single stage microchannel plate (MCP) image intensifier. The phosphor of the intensifier is coupled to a CCD by a tapered fiber optics bundle. The CCD is read out at a fast rate ~ 30 frames per second. The WIC CCD electronics analog to digital converter converts the video to digital data. These data are transferred to the WIC TDI board located in the MEP. There are two separate high voltage power supplies for the WIC, one for the MCP with negative output and another for the phosphor with positive outputs. Both high voltage power supplies are programmable. The WIC Camera has an aperture door, that is used to minimize contamination before and post launch. The door can be opened on command once only. There are also heaters in the WIC camera. One heater is mounted on the last baffle to warm the secondary mirror and it's mounting structure. This was necessary to minimize the amount of defocusing, which was observed in calibration when the optics was cooled. There are several thermistors to read out the instrument temperatures. The WIC instrument is described in a companion paper (Paper 2).

IMAGE FUV Block Diagram

3/20/99

10
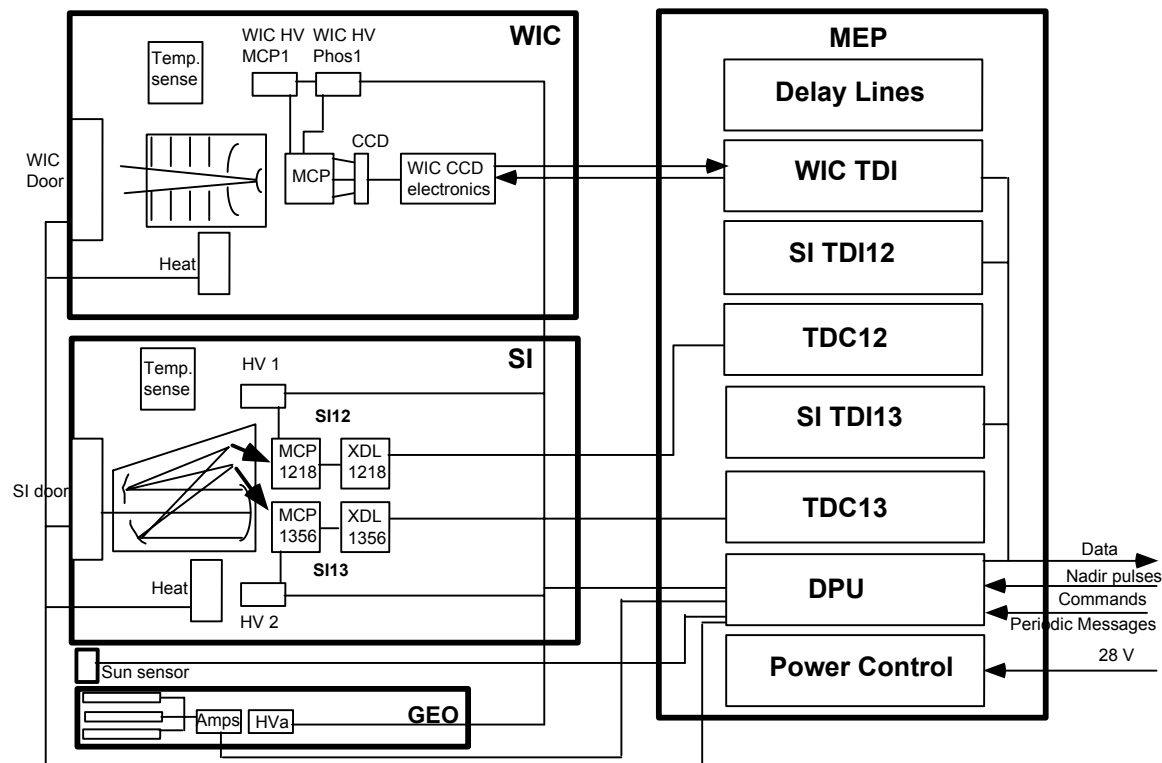
Figure 3. FUV instrument block diagram, the four packages are the Wideband Imaing Camera (WIC), the Spectrographic Imager (SI), the GOcoronal photometer (GEO) and the Main electronics Package (MEP).

The Spectrographic Imager (SI), which is described in another companion paper (Paper 3), consists of a large optical cavity containing the grating and several mirrors. There are two wavelength channels; one is for the Doppler-shifted Lyman-α wavelength region and the other is for the OI 135.6 nm line vicinity. The SI is essentially a monochromatic imager forming two-dimensional images on the detectors in selected pass-bands. In the Lyman-α channel there are special grills that operate in anti-coincidence to filter out the cold geocoronal Lyman-α at 121.5667 nm. There are two independent detectors for the two wavelength regions. Each detector consists of a MgF_2 entrance window followed by a triple MCP stack. Each detector has a separate high voltage power supply to power the MCP. The output of each MCP is read out by an anode array, which operates by the Time Delay Conversion (TDC) principle, in which the position of each photoelectron incidence is encoded and this position is used as an address to increment a memory location on the TDI boards. There is a set of TDC and TDI electronics for each detector. The SI also has heaters and temperature sensors and a door to minimize the entry of contaminants.

The GEO instrument contains 3 separate Lyman-α detector tubes with individual MgF_2 lenses to detect Lyman-α. There is a common high voltage supply for the three tubes. The output of the GEO tube pre-amplifiers is connected to the DPU where the pulse counters and storage registers are housed. The GEO instrument also houses 4 sun sensors, which are used to protect the instruments by turning the HV down on the FUV instruments when directly illuminated by the sun.

There are 2 visible and 2 ultraviolet sun sensors. The usage logic of the various sun sensors can be programmed during flight. The sun sensors set the high voltages to a programmable level through hardware only. This means that when the sun is in the field of view the high voltage supplies are commanded on the sun-up state. In this state, the programmed high voltages are set low– generally on the order of 200 volts, insufficient to cause harm to the instrument. The same type of high voltage supplies were used on the FAST spacecraft, where they have been operating in this mode for several years to produce rapid high voltage ramps for electrostatic analyzers. During certain orbital configurations of IMAGE, we propose to switch once per satellite revolution. Based on the FAST heritage this should not be a problem.

The MEP is shown on the right side of Figure 3. In reality, the MEP is a stack of modules. The delay line module holds the delay line cables needed to separate the start and stop pulses in the SI TDC circuitry. The WIC TDI board contains the WIC memory, which is used to integrate the WIC images during WIC exposures.

The whole system is controlled by the DPU, which initiates the data transfer to the payload's Central Instrument Data Processor (CIDP). The DPU receives a synchronization pulse each rotation, which is called the nadir pulse. It is known that the FUV imagers are located 315° from the spacecraft nadir and the nadir pulse is used to initiate the FUV data taking. The rotation rate as determined by the spacecraft star tracker is transmitted to the FUV DPU as part of a Periodic Message from the CIDP to the DPU. The FUV DPU also receives commands from the CIDP. Since the Earth can be observed for a maximum of 20 seconds per spin, substantial power saving is realized by turning off some instrument components when they are not needed. The power controller regulates and switches the power to the various FUV subsystems. The average power used by the IMAGE FUV system is less than 13 W. This does not include survival or other heaters.

Table 2
Instrument design parameter summary, SI

Instantaneous FOV	15° x 15°
Memory field	15° x 15°
Number of memory pixels	128 x 128
Wavelength pass-band SI12 channel	119 – 126 nm not at 121.5667 or at 120.0
Wavelength pass-band SI13 channel	135.6 +- 4.0 nm
Optics	2-D imaging monochromator
Detector type	Crossed delay line (single event counter)

WIC

Instantaneous FOV	30° x 17°
Memory field	17° x 17°
Number of memory pixels	256 x 256

11

Wavelength pass-band	140 – 190 nm
Optics	Concentric reflective system
Detector type	MCP phosphor coupled to CCD

GEO	
Instantaneous FOV	$1°$ circular
Field Coverage	$360°$
Number of channels	3
Wavelength pass-band	115 – 190 nm
Optics	MgF2 lens
Detector type	Channel electron multiplier

4. TDI Operation and Distortion Correction

As previously stated, the restricted telemetry and data storage requires image motion compensation correction to be applied in real time for each spacecraft spin for the two SI channels and the WIC. The first step in the image processing is to remove the imager distortion. The image can be represented by a matrix, and each pixel has angular coordinate x_0, y_0 that denotes a direction in inertial space. Since the imager distorts the image, the corresponding pixels in the imager pixel matrix x_1, y_1 are related according the following pair of equations:

$x_1 = f_1 (x_0, y_0)$ and $y_1 = f_2 (x_0, y_0)$.

The rotation correction consists of re-mapping the pixel matrix by adding an angular offset equal and opposite to the rotation. Since the rotation angles apply only in inertial space it is necessary to re-map the images back to their original, undistorted inertial positions, i.e. into the frame represented by x_0, y_0.

In the IMAGE FUV system this distortion correction is accomplished by using a look up table, which for each detector space pixel coordinate x_1, y_1 (address), returns a new coordinate x_2, y_2 (look up table content). This latter value is used as the coordinate for storing the pixel intensity value. It is possible to build circuitry that does the transposition at the speeds required by the fast-framing WIC camera based on the lookup table scheme. In a general sense, the relationship between the new and old coordinate systems can be expressed as:

$x_2 = F_1 (x_1, y_1)$ and $y_2 = F_2 (x_1, y_1)$.

If the distortion correction is successful, then $x_2 = x_0$ and $y_2 = y_0$ and the transformations represented by functions F are the inverse of function f. The functions F_1 and F_2 had to be determined by prior calibration measurement. Collimated beams were directed to the imager at various known angles representing values of x_0 and y_0 and the corresponding pixel values x_1 and y_1 were determined. From this data set we determine the coefficients in a power series expansion to obtain the functional form of F_1 and F_2. The coefficients for the power series expansion (polynomial) are up-linked to the instrument as commands and then x_2 and y_2 values are calculated for each detector pixel x_1, y_1. The results of these calculations are used to fill up the entire look up table. Once the look up table filling is completed the instrument can find the appropriate x_2 and y_2 value rapidly at full video rates. The distortion polynomials for the functions F_1 and F_2 were chosen as:

For the SI the corrected space x_2 and y_2 are given as:
$$x_2 = A_0 + A_1 x_1 + A_2 y_1 + A_3 x_1 y_1 + A_4 x_1^2 + A_5 y_1^2 \ ; \qquad \text{(i)}$$
$$y_2 = B_0 + B_1 x_1 + B_2 y_1 + B_3 x_1 y_1 + B_4 x_1^2 + B_5 y_1^2 \ ; \qquad \text{(ii)}$$

for WIC:
$$x_2 = A_0 + A_1 x_1 + A_2 y_1 + A_3 x_1^2 + A_4 y_1^2 + A_5 x_1 y_1 +$$
$$A_6 x_1^3 + A_7 x_1^2 y_1 + A_8 x_1 y_1^2 + A_9 y_1^3; \qquad \text{(iii)}$$
$$y_2 = B_0 + B_1 x_1 + B_2 y_1 + B_3 x_1^2 + B_4 y_1^2 + B_5 x_1 y_1 +$$
$$B_6 x_1^3 + B_7 x_1^2 y_1 + B_8 x_1 y_1^2 + B_9 y_1^3 \ ; \qquad \text{(iv)}$$

An important part of the IMAGE FUV calibration was producing enough data to be able to calculate coefficients A_i and B_i.

The distortion correction re-maps the entire image. There are regions where the image has to be compressed and other regions where the image has to be expanded. Furthermore, in general the information has to be distributed between several adjacent pixels according to which part of the original pixel was activated by the incoming photon. For example, in Figure 4d, the photons arriving in the shaded areas will be put into one of the four destination pixels shown. Thus, it would be ideal to divide the charge package according to the location of the centroid of the package relative to the boundary of the adjacent pixels and sum the correct amount of charge into each pixel. Such processing could not be performed at the speeds required by the WIC TDI process. If one were to ignore this issue, then a uniformly illuminated object would show patterns because certain destination pixels in the set would always receive information whereas others would never be illuminated. The imager does not have the information regarding which part of the pixel the photon originates from because that would require sub-pixel resolution. In the case of the SI, where the final image is 128x128 but the detector intrinsic resolution is 1024x1024, we process the TDI correction at sub pixel resolution. In case of the WIC, however, the resolution is barely adequate to produce the 256x256 raster. To overcome this difficulty, the signal information is put each time into a single pixel of the destination set, but we vary the chosen pixel each time according to a probability distribution defined by the sizes of the overlap in the areas. This approach was chosen because the process has to be executed at CCD pixel read out rate (100 ns) in hardware, and this approach results in a simple algorithm. Actual implementation is as follows. Although only 8 bits were required for the 256 x 256 WIC output image, the look-up table contents were 12 bit addresses, representing 12 bit accuracy, for x and y. The computation of the rotation rates and the arithmetic adding of the rotation offset also takes place with 12 bits accuracy and the resulting destination pixel address has 12 bits accuracy. Before truncating it to 8 bits, however, a number between 0 and 15 is added to "randomize" the resulting truncated 8 bit number. The number is incremented from 0 to 15 for each new CCD frame. This way the pixels which are added in memory produce a distortion compensated 256 by 256 picture raster which fills in all the pixels with a uniformity of less than 1 unit in 16.
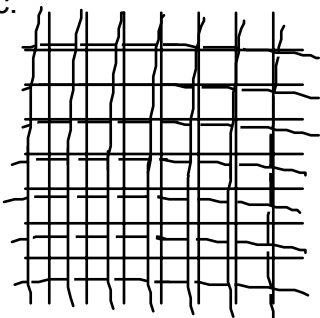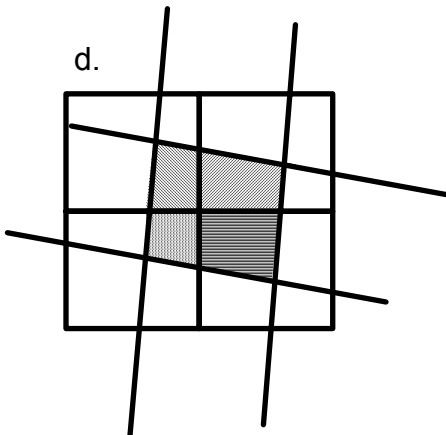
a.

b.

c.

d.

13
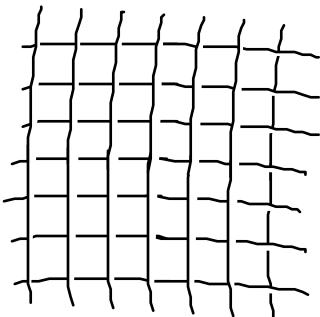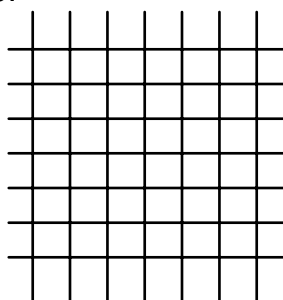
Figure 4. Principle of distortion correction. a) Distorted raster sourceat the output of the imager, b) True rectilinear raster, as it should be in the distortion corrected destination raster, c) Superimposition of the two, and d) an example how a source pixel needs to be mapped into several adjacent destination pixels.

The distortion correction hardware/software and the rotation correction system were tested by using the WIC camera Engineering Test Unit (ETU) mounted on a rotating platform. The ETU was nearly identical to the flight unit electronics and CCD except a simple visible lens was attached in place of the UV front end to form an image on the CCD in visible light. A distorting convex mirror was introduced into the system so that when the system viewed a rectilinear grid the image appeared substantially distorted. The distortion was calibrated by assigning the true angular coordinates to the distorted pattern points and allowing the system to correct these distortions. The raster as imaged by the system through the distorting mirror is shown as Figure 5a. Coordinates x_0 and y_0 were assigned to the angles which were subtended by the points of intersection of the grid lines. For each intersection we recorded the corresponding pixel value (x_1,y_1) in the distorted image (Figure 5a). The corresponding sets of coordinate pairs x_0, y_0 and x_1,y_1 were used to determine coefficients A_0 to A_9 in equation (iii) and (iv).
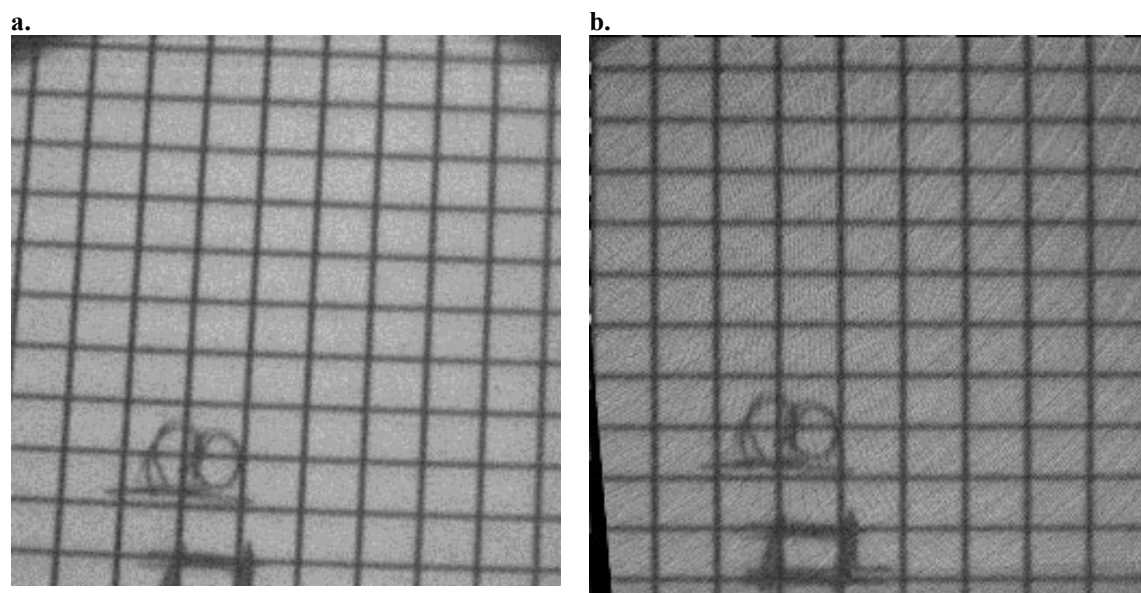
a.

b.

Figure 5. Test of the distortion correction software and hardware. a) Original image taken with the WIC ETU CCD through a distorting mirror using a pixel look up table with 1 to 1 addressing. This produces an image without distortion correction. b) When the appropriate look up table is applied to the image correct for the combined distrotion of mirror optics and camera.

To perform the test, the calculated coefficients were "uplinked" to the MEP and the DPU was commanded to execute the algorithm and store the look up table based on the uplinked coefficients. Once the look up table computation was finished the instrument was commanded into data taking mode and the images were corrected at real time video rate. The corrected real time image of the distorted pattern is shown in Figure 5b. The computations showed that the technique provided a least square fit accuracy, which was much less than .5 pixel even at the worst case locations. Figure 5 shows that the grid has become much more rectilinear showing the effectiveness of the FUV real time video look up table processor. As it was discussed earlier, certain pixels receive more or less signal depending on the distortion mapping algorithm. To minimize this effect the "randomizer" was used. Although there is still some residual patterning in the image intensity due to the imperfection of the signal distribution, it is much reduced in amplitude because of the randomizer. We expect that the maximum intensity modulation should be 1/16 of the full range when the randomizer is on. In TDI operation with a moving imager, this type of pattern generation manifests itself as an additional image non-uniformity, which is smoothed in the direction of the motion.
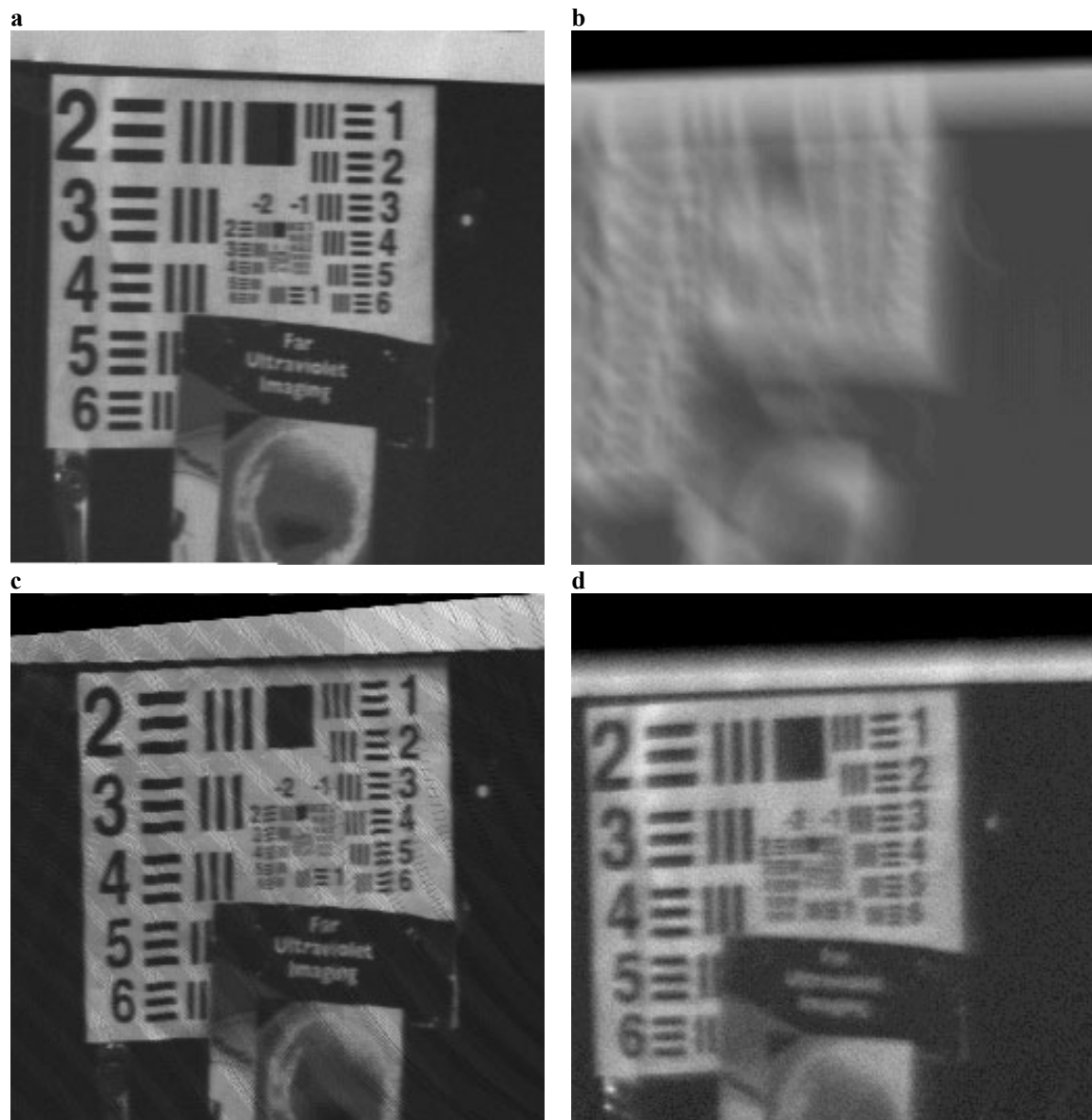
a
b
c
d

Figure 6. Images taken from a still and a rotating platform and the application of distortion correction.   a) Resolution pattern as seen by the ETU imaging system with the distortion producing mirror while using a non-corrected 1 to 1 look up table, b) same as (a) except the camera platform is rotating from right to left during the exposure emulating spacecraft rotation and the image is collected in the TDI mode, c) non-rotating camera imae with distortion correction applied and d) image taken in the TDI mode with distortion correction also applied.

To verify the end-to-end software and electronics system performance, the imager, including the distorting mirror, was mounted on a one-axis rotating platform. The results of operating the system are shown in Figure 6. The pictures at left were taken while the platform was stationery (n frame integration) and the right ones were taken when the platform was rotating about a vertical axis counter clockwise at 3° per second (1000 frame integration). The IMAGE nominal rotation period is two minutes (= 3° per second). Figures 6a and 6b were taken when the look up table was one to one i.e. $x_1 = x_0$ and $y_1 = y_0$. When taking the bottom row, we used the look up table derived from generating Figure 5.

The resolution in the image shown in Figure 6a is only limited by the camera, therefore it appears to be the sharpest. Figure 6c is essentially the same except that the distortion correction was applied. Regions which have uniform illumination in the image of 6a show faint patterns due to the effects discussed above. If the distortion

correction is not applied and an image is taken while the imager is on a rotating platform then the result is 6b, which is greatly blurred. If the distortion correction is applied and the image is taken while the platform is in motion, then we obtain the image shown in Figure 6d. The improvement is remarkable, although there is still some blurring through the TDI process.

It is possible to sharpen the image by reducing exposure time. Regions nearer the corners of the imager produce much more distortion than in the center of the image. To illustrate that improvement can be realized by eliminating regions away from the center, the following experiment was performed. We added a feature to the distortion correction look up table that blanks the left and right side of the image. The resulting direct image taken by the camera is shown on Figure 7a. When the instrument was operated in the TDI mode Figure 7b was produced. When compared to 6d this demonstrates that by blanking the outlying parts of the image one can sharpen the image. The trade off is a reduction of the effective exposure time because with the reduced field of the imager a region of the Earth would spend less time in the field of view of the camera, but as we have seen the resolution can be enhanced substantially. The blanking of the detector was accomplished by uplinking a special test look up table which nulls the data in the outlying regions. This operation can be performed while IMAGE is on orbit. We hope that we do not have to use this technique to sharpen up the images but it does provide a back up option to minimize the reliance on the distortion correction algorithm.
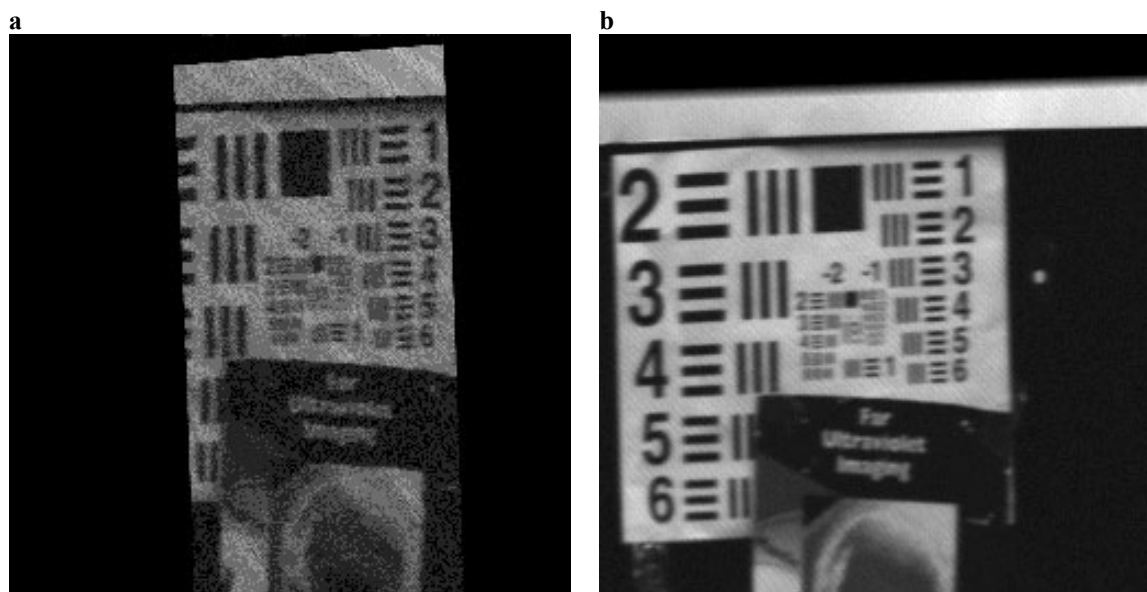

Figure 7. Improvement in resolution by using only the central region of the imager. a) The left and right parts of the detector are blanked by the look up table and the distortion correction is applied to a stationery camera image, b) image collected in the TDI mode while the cmera is rotating and using the same banking as in a).

The TDI circuits are also part of the SI data processing chain. The SI data is processed with full 12 bit spatial resolution so the distortion correction produces minimal undesirable fringes. Note that the intrinsic detector resolution of the SI is about 30 microns, which is linearly 4 x 4 times better than what is needed. Once again, the distortion-corrected addresses are modified by an offset computed from the spacecraft rotation and a single 128 x 128 pixel image is integrated per rotation.

5. System Performance Validation

The IMAGE FUV system was built in a relatively short time period by a team that included several institutions. The IMAGE FUV contract was awarded in June 1996 and the FUV flight instrument complement was delivered for integration in January 1999. The SI was designed jointly by the Centre Spatiale of the University of Liege in Belgium and by UC Berkeley and Lockheed-Martin. It was built and calibrated entirely in Liege. The WIC optics was imported from Canada and was integrated at UC Berkeley into the flight unit, which was built at UC Berkeley. The WIC was tested and calibrated by NASA Marshall Spaceflight Center in Huntsville, Alabama. The GEO tubes

were supplied by the Max Planck Institut fur Aeronomie, Lindau, Germany and were integrated into the flight electronics package at UC Berkeley. The WIC and GEO integration and the Main Electronics Package design and construction were all done at Berkeley. In order to accomplish the extensive amount of work on schedule, the various institutions were working in parallel and the various sense heads were built and calibrated at their separate institutions. The calibrations were supported by special purpose ground support electronics and not by the flight Main Electronics Package unit.

The FUV instrument complement will operate on a rotating spacecraft and we did not have rotating platforms available in the calibration vacuum chambers. Therefore, each instrument was tested and calibrated as a stationery imager. When the instruments were integrated with the flight Main Electronics Package the calibrations were checked but once again in a stationery state when the imagers were still in a staring mode.

In actual, on-orbit performance, the imagers will perform an averaging process in the TDI direction. The actual flight instruments could not be exercised on a rotating platform and much of the software development and the calibration interpretation had to be based on the behavior of engineering test units which were operated in the TDI mode on a rotating platform.

The individual instrument performance and instrument calibrations are discussed in the companion papers. It is our objective to summarize the results here to show that IMAGE FUV has met the requirements of the IMAGE science objectives.

Table 3
IMAGE FUV Instrument Performance Summary

	Pixel Size (^{o})	Resolu-tion cell size (^{o})	Resolu-tion cell at apogee (km)	Resolu-tion cell at perigee (km)	Photon Collection (cm^{-2} R^{-1} $cell^{-1}$)	Measured equivalent aperture A_e (cm^2)	Counts $cell^{-1}$ / 100 R/exposure
GEO	1.0	1	667	17	6.3	0.019	12
WIC	0.09	0.18	120	3.1	5.7	0.04	23
SI 1218	0.11	0.11	73	2	1.6	0.010	1.8
SI 1356	0.11	0.11	73	2	1.6	0.008	1.3

The instrument parameters are summarized in table 3. The second column is the pixel size, the angular area associated with one memory element. The third column is the resolution cell size, which is the resolution full width at half maximum of the measured point spread function. On the WIC this quantity is approximately twice the pixel diameter. On the SI the optical and detector resolution is less than the pixel size, therefore, we used the pixel size as the resolution cell size. The GEO is a fully-baffled, single channel photometer and the measured angular response is very close to the nominal, so we used one degree as the resolution cell size. The fourth and fifth columns represent the resolution cell size projected to the ground at apogee and perigee. The resolution cell size defines the solid angle from which photons are collected and allows us the calculation of the photon collection efficiency per cm^2 during the exposure time. This is presented in column six. Column seven is the equivalent aperture A_e of each system as discussed earlier. This combined with the photon collection efficiency provides the number of significant quanta (column 8) per 100 Rayleigh source within the resolution cell of the instrument for a single spin of the spacecraft. Column seven, A_e, can be compared directly to the values in Table 1.

6. Data Products

The FUV data consist of packages containing SI12, SI13 and WIC images, three GEO data sets, periodic message data forwarded from the IMAGE Central Instrument Data Processor (CIDP) and housekeeping. The periodic messages contain vital data for FUV to process the images.

For successful TDI-ing, the FUV software needs to have the accurate instantaneous TDI rate in the direction of the imager's x and y coordinates. The direction of rotation correction should be closely aligned with the imager x axis and only minimal correction should need to be applied in the y direction. The angle α between x and y, is the quantity that defines the direction of the TDI rotation correction. For calculating α we need to know the position of the satellite rotation axis and the true location of the imager on the satellite. It is our intention to assume that α is a constant and calculate these parameters from star tracker data and pre-launch measurements.

The periodic message data contain all the parameters needed for the calculation including the direction of the rotation axis in the inertial frame. The periodic message also contains the instantaneous spin rate. This latter

quantity is used directly by the DPU for generating the TDI speed rates on orbit. The TDI process requires an accuracy of 0.5% or better to stay in synch with the rotation rate and co-add 128 pixels.

A much more stringent requirement is the absolute knowledge of where the instrument is mapping the memory, which represents inertial space. For this information we need to determine the absolute instantaneous look angle. The satellite star tracker will provide this information in real time. Unfortunately, relating the directional offset between the star tracker data and our imager view direction might be difficult. Even if extensive measurements are made about the relative locations of these two sub-systems pre-launch, the FUV camera and the star tracker, the launch environment will probably disturb the positions and invalidate the measurements. It is, therefore, very important to make periodic location checks by observing stars in the field of view. By using the data for the instrument offset it is possible to predict where stars should be observed. We can correct the offset by comparing the measured and the actual location of certain stars. It should be noted that IMAGE true polar orbit should not precess in inertial space and the same set of stars should be observed on every spin during its orbital life. The FUV has observing modes for star observations by offsetting the view angle from the nadir.

The data taken by the IMAGE satellite will be put on the World Wide Web and will be distributed publicly. The format of the IMAGE FUV browse products is schematically illustrated in Figure 8. The digital data will also be available in common data format (CDF) and similar formats that allow downloading and subsequent processing.
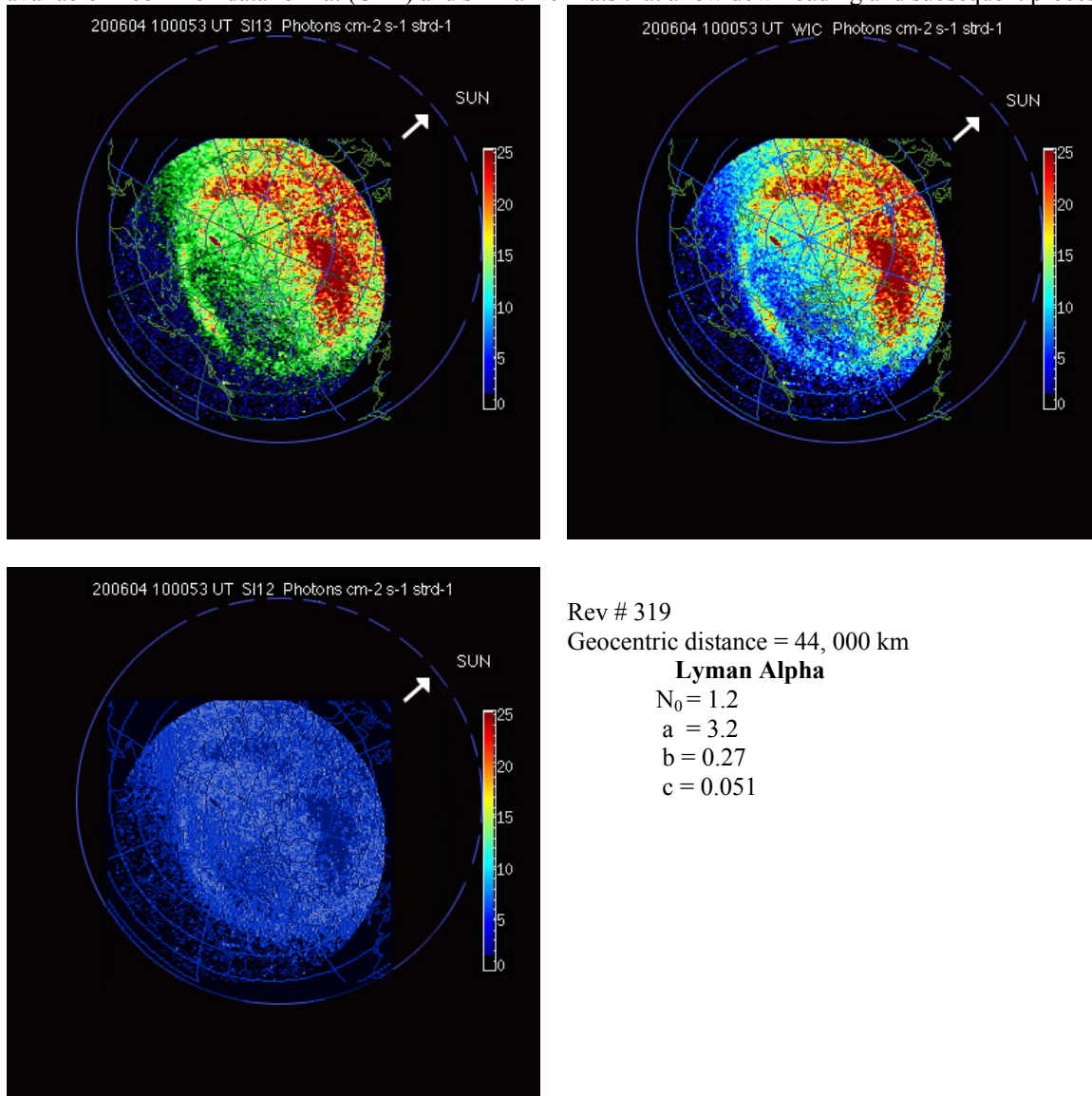

Rev # 319
Geocentric distance = 44, 000 km
Lyman Alpha
$N_0 = 1.2$
$a = 3.2$
$b = 0.27$
$c = 0.051$

Figure 8. Proposed IMAGE FUV browse products. The images are taken from POLAR UVI and represented at a size in

proportion to the IMAGE FUV fields of views. Note IMAGE FUV field of view is larger than POLAR UVI field. The fourth panel is a schematic representation of the parametric information, which will be provided from the geocoronal photometer measurements.

The FUV browse products represent the actual view of the Earth as seen by the imagers. In Figure 8 we have used POLAR UVI images for illustration. These images are about a half of the field of view of the IMAGE FUV instruments and the grid drawn around them represents the size of the Earth in the FUV images.   We will superimpose the geographic grid on the images during ground processing. The data needed to project the Earth grid will be down-linked in the housekeeping data. These data consist of: start and stop time of image TDI, accurate rotation rate from the IMAGE star tracker, time of the satellite axis pointing at nadir, star tracker look angle quarternions, and direction of the satellite spin axis. Some other data, such as the instrument angular coordinates in the satellite frame of reference, will be determined from pre-launch calibration and on orbit observation of stars in the field of view.

The preflight calibration data will be used to reduce the raw digital numbers into geophyiscal units.   The housekeeping data contain a number of key data sets which will aid in performing this conversion. For example, the housekeeping data contain temperature and applied voltages including the output of the high voltage power supplies. Also, the SI detectors continuously down-link sample pulse height distributions. By adjusting the high voltages it is possible to compensate for MCP gain changes and recover the initial pulse height distributions. The WIC pulse height distributions can be recovered by stopping the TDI process and recovering images from single frame exposures.   In addition, periodic imaging of FUV stars will create an important data set for monitoring the sensitivity of the imagers. The GEO detector data will be in the form of model parameters and no image will be produced.

Acknowledgements

References

Ajello, J. M., Solar minimum Lyman-α sky background observations from Pioneer Venus orbiter ultraviolet spectrometer: Solar wind latitude variation, *J. Geophys. Res.*, **95**, 14855-14861, 1990.

Anger, C. D., S. K.Babey, A. Lyle Broadfoot, R. G. Brown, L. L. Cogger, R. Gattinger, J. W. Haslett, R. A. King, D. J. McEwen, J. S. Murphree, E. H. Richardson, B. R. Sandel, K. Smith and A. V. Jones, An ultraviolet auroral imager for the Viking spacecraft, *Geophys. Res. Lett.,* **14**, 387, 1987.

Bishop, J., Transport of resonant atomic hydrogen emissions in the thermosphere and geocorona: Model description and applications, *J. Quant. Spectrosc. Radiat. Transfer*, **61**, 473, 1999.

Coroniti, F. V. and C. F. Kennel, Changes in magnetospheric configuration during the substorm growth phase, *J. Geophys. Res.,* **19**, 3361, 1972.

Drob, D. P., R. R. Meier, J. M. Picone, D. J. Strickland, R. J. Cox and A. C. Nicholas, Atomic oxygen in the thermosphere during the July 13, 1982, solar proton event deduced from far ultraviolet images, *J. Geophys. Res.,* **104**, 4267, 1999.

Frank, L. A., J. D. Craven, K. L. Ackerson, M. R. English, R. H. Eather and R. L. Crovillano, Global auroral imaging instrumentation for the Dynamics Explorer mission, *Space Sci. Instrum.,* **5**, 369-393, 1981.

Frank, L. A. and J. D. Craven, Imaging results from Dynamics Explorer 1, *Rev. of Geophys.,* **2**, 249, 1988.

Frank, L. A. and J. B. Sigwarth, Atmospheric holes: Instrumental and geophysical effects, *J. Geophys. Res.,* **104**, 115, 1999.

Fuselier, S. A., D. M. Klumpar and E.G. Shelley, Ion reflection and transmission during reconnection at the Earth's subsolar magnetopause, *Geophys. Res. Lett.,* **18**, 139, 1991.

Gladstone, G. R., Simulations of DE-1 UV airglow images, *J. Geophys. Res.,* **99**, 11,441, 1994.

Hodges, R. R., Monte Carlo simulation of the terrestrial hydrogen exosphere, *J. Geophys. Res.,* **99**, 23,229, 1994.

Hunten, D. M., F. E. Roach, and J. W. Chamberlain, A photometric unit for the airglow and aurora, *J. Atmos. Terr. Phys.*, **8**, 345-346, 1956.

Immel, T. J., J. D. Craven and L. A. Frank, Influence of IMF By on large-scale decreases of O column density at middle latitudes, *J. Atmos. Terr. Phys.,* **59**, 725, 1997.

Jorgensen, A. M., H. E. Spence, M. G. Henderson, G. D. Reeves, M. Sugiura and T. Kamei, Global energetic neutral atom (ENA) measurements and their association with the Dst index, *Geophys. Res.. Lett.*, **24**, 3173-3176, 1997

Lockwood, M., M. O. Chandler, J. L. Horowitz, J. H. Waite, Jr., T. E. Moore and C. R. Chappell, The cleft ion foundation, *J. of Geophys. Res.,* **90**, 9736, 1985.

Lui, A. T. Y., D. Venkatesan and J. S. Murphree, Auroral bright spots on the dayside oval, *J. Geophys. Res.,* **94**, 5515, 1989.

Lui, A. T. Y., D. J. Williams, E. C. Roelof, R. W. McEntire and D. G. Mitchell, First composition measurements of energetic neutral atoms, *Geophys. Res. Lett.*, **23**, 2641-2644, 1996.

Meier, R. R., Ultraviolet spectroscopy and remote sensing of the upper atmosphere, *Space Sci. Rev.,* **58**, 1, 1991.

Murphree, J. S., R. A. King, T. Payne, K. Smith, D. Reid, J. Adema, B. Gordon and R. Wlochowicz, The Freja Ultraviolet Imager, *Space Science Reviews,* **70**, 421-446, 1994

Pollock, C. J., M. O. Chandler, T. E. Moore, J. H. Waite, Jr., C. R. Chappell and D. Gurnett, A survey of upwelling ion event characteristics, *J. Geophys. Res.,* **95**, 18969, 1990.

Rairden, R. L., L.A. Frank and J. D. Craven, Geocoronal imaging with Dynamics Explorer, *J. Geophys. Res.,* **91**, 13,613, 1986.

Roelof, E. C., Energetic neutral atom image of the storm time ring current. *Geophys. Res. Lett.*, **14**, 652, 1987.

Roelof, E. C., D. G. Mitchell and D. J. Williams, Energetic neutral atmos (E ~ 50 keV) from the ring current: IMP 7/8 and ISEE 1, *J. Geophys. Res.*, **90**, 10,991, 1985.

Strickland, D. J. and D. E. Anderson, Jr., Radiation transport effects on the OI 1356-AA limb intensity profile in the dayglow, *J. Geophys. Res.,* **88**, 9260, 1983.

Strickland, D. J., J. P. Jasperse and J. A. Whalen, Dependence of auroral FUV emissions on the incident electron spectrum and neutral atmosphere, *J. Geophys. Res.*, **88**, 8051-8062, 1983.

Strickland, D. J., R. E. Daniell, Jr., J. R. Jasperse and B. Basu, Transport-theoretic model for the electron-proton-hydrogen atom aurora, *J. Geophys. Res.,* **98**, 21533, 1993.

Strickland, D. J.; J. S. Evans, L. J. Paxton, Satellite remote sensing of thermospheric O/N_2 and solar EUV. 1. Theory, *J. Geophys. Res.*, **100**, 12,217-122,26, 1995.

Strickland, D. J., R. J. Cox, R. R. Meier, and D. P. Drob, Global O/N2 derived from DE-1 FUV dayglow data: Technique and examples from two storm periods, *J. Geophys. Res.,* **104**, 4251, 1999.

Torr, M. R., D. G. Torr, M. Zukic, R. B. Johnson, J. Ajello, P. Banks, K. Clark, K. Cole, C. Keffer, G. Parks, B. Tsuratani and J. Spann, A far ultraviolet imager for the International Solar-Terrestrial Physics mission., *Space Science Reviews*, **71**, 329, 1995.

Williams, D. J., E. C. Roelof, and D. G. Mitchell, Global magnetospheric imaging, Reviews of Geophysics, **30**, 183-208, 1992.

Williams, D. J., Why we need global observations, in Magnetospheric Physics, edited by B. Hultquist and C. G. Falthammer, pp. 83-101, Plenum, New York, 1990.